CFD and Experimental Study of Forebody Vortex Interactions with the Tail Fins

James DeSpirito
U.S. Army Combat Capabilities Development Command–Army Research Laboratory
Aberdeen Proving Ground, Maryland 21005
USA

james.despirito.civ@mail.mil

Roopesh Kumar and Rajan Kumar
Florida Center for Advanced Aero-Propulsion
Florida A&M University-Florida State University College of Engineering, Tallahassee, Florida 32310
USA

roopesh280588@gmail.com, rkumar@fsu.edu

ABSTRACT

A combined experimental and numerical study was performed to gain a better understanding of the development of vortices over a slender body configuration at a range of incidence angles. The experiments were performed at the Florida A&M University-Florida State University low-speed wind tunnel and numerical simulations were performed at U.S. Army DEVCOM - Army Research Laboratory using the Kestrel/KCFD solver. Normal force characteristics show a monotonic increase with incidence angle while the side force variation is periodic. Particle image velocimetry and computational fluid dynamic simulations show that asymmetric vortices develop on the cone cylinder and interact with the tail fins downstream at moderate incidence angles. The primary vortices eventually lift off from the body resulting in the formation of multiple secondary shear-layer vortices. The secondary vortices can interact with the tail fins at the larger incidence angles. The lift-off location moves upstream with an increase in incidence angle. The dissimilar lift-off location between the two primary vortices leads to a switch in the side force magnitude and direction. The results show a reasonable agreement of basic aerodynamic characteristics between the experimental data and numerical simulations at incidence angles up to 20°. Above this angle, the lateral loads were qualitatively similar in form, but differences in peak numerical values and phase affected all the aerodynamic coefficients to some degree. The predicted numerical vorticity fields look qualitatively similar to those from the experiment but there is a mismatch in the initiation of the vortex asymmetry leading to the peak value and phase differences.

1.0 INTRODUCTION

The flight stability and maneuverability of missiles and projectiles can be affected by the interaction of vortices with the vehicle surfaces and lead to adverse roll or yaw moments. One type of interaction is caused by vortices shed from upstream control surfaces (e.g., wings, strakes, or canards) in which the induced velocity field affects the pressure distribution on a set of tail fins. This type of vortex interaction primarily affects the vehicle roll moment and sometimes even leads to reverse roll [1–3]. For example, forebody canards generate vortices when deflected for pitch, yaw, or roll control. With canards deflected for pitch control, the tip vortices generated are symmetric and induce a downwash on the tail fins leading to a negative, nose-down pitching moment that enhances control authority (and reduces maneuverability). However, with canards deflected for roll control, the

vortices generated from canards interact with tail fins and induce a roll moment that can oppose the canard-commanded roll moment. If the roll moment produced from the tail fins is large, it can cause an adverse rolling moment or a roll-reversal. This unfavorable rolling moment is a strong function of tail fin span and surface area [2]. This type of vortex interaction effect is reduced as the angle of attack, α, increases such that the vortex tubes travel past the tail fins at a greater distance.

A second well-known interaction effect is a strong yaw moment ("phantom yaw") induced by asymmetric vortex shedding from the vehicle body, usually the forward (nose, ogive, or cone) section, that generates large (on the order of the normal force) side forces on the vehicle body. The asymmetric vortex interaction usually does not occur until larger angles, usually when α is greater than about twice the half-angle of the nose. At moderate angles, a pair of symmetric vortices are usually shed that do not induce any side loads but may either reduce or enhance the stabilizing effect of the tail fins. Figure 1 shows examples of symmetric and asymmetric body-shed vortices. For the case in Figure 1a, as the incidence angle increases, the attached flow rolls up into a symmetric vortex pair at moderate angles. As the incidence angle increases further, the separation becomes asymmetric, producing large side forces and moments of the same order as the longitudinal loads.

(a) Symmetric Vortex (b) Asymmetric Vortex

Figure 1: Schematic of the forebody vortex interaction with control surfaces.

The magnitude and direction of side force for a given configuration depend on the Mach number, Reynolds number, angle of attack, and orientation of the forebody. Several studies [4–10] have reported that the vortex asymmetry is initiated by random surface imperfections near the forebody tip that further develops along the length of the body resulting in adverse yaw moments. In addition to these micro-surface imperfections, freestream turbulence, vortex flow instabilities, and a combination of all have shown importance, making this a difficult problem both experimentally and computationally. At moderate incidence angles, the vortices are symmetric, reside close to the body, and therefore interact with the control surfaces as they move downstream. This interaction can significantly affect the performance of control surfaces positively or negatively depending upon the vortex strength, orientation, and location with respect to the control surface. At high incidence angles, the vortices are asymmetric with one vortex lifted-off from the body and the other residing close to the body resulting in net side force [11-12]. The potential for the adverse loadings caused by these interactions makes understanding flow physics and accurate prediction capability very important.

From the above discussion, it is evident the flow over a slender body at high incidence angles becomes complex, where the flow field can change dramatically at each incidence angle. Most of the previous studies on a long slender body were limited to examining the flow field locally to specific incidence angles using PIV, numerical simulation, or other flow visualization techniques. However, the fundamental questions regarding the development and interaction of the vortices along the body at varying incidence angles remain unanswered. The

present investigation aims to study the effect of incidence angle on the location, size, and strength of forebody vortices and the resulting changes in the aerodynamic forces and moments.

A joint study was commenced to investigate the vortex interference effects due to both symmetric and asymmetric vortices. The experimental study was performed at both subsonic and supersonic conditions in the wind tunnel facilities at the Florida A&M University (FAMU)–Florida State University (FSU) College of Engineering and the computational fluid dynamic (CFD) study was performed at the U.S. Army Combat Capabilities Development Command (DEVCOM)–Army Research Laboratory (ARL). The aim of the present investigation is to study the effects of forebody vortex interactions on control surfaces and the effect of vortex asymmetry on control surface effectiveness. The flow development is studied using planar Particle Image Velocimetry (PIV), Schlieren, and the resulting forces experienced by the body are measured using an internal strain gauge balance. Numerical simulations were performed using the Department of Defense (DOD) High-Performance Computing Modernization Program's (HPCMP) CREATE™-AV Kestrel computational physics suite.

The study was conducted in two phases, one in the supersonic regime at Mach 2.0 and incidence angle up to 12° [13] and one in the subsonic regime (~Mach 0.1) at incidence angles up to 60° [14]. Asymmetric vortices were not generated in the limited incidence angles achieved in the Mach 2.0 case. Surface oil-flow visualizations and CFD flow field visualizations showed that at a 12° angle of attack, the flow separates toward the mid-section to form a pair of symmetric vortices. The vortex pair grows along the length of the body and interacts with the fins downstream. Since the vortices are symmetric, no side force or yaw moments are generated, but analysis showed that the vortices affect the resulting pressure distribution over the fins. As this can adversely affect the stability and maneuverability of the vehicle, it demonstrates the importance of accurately measuring or predicting the vortex interaction.

This paper will focus on the subsonic, high angle of attack case that resulted in significant lateral loads due to asymmetric vortex shedding. A computational study of the wind tunnel model and sting section using the wind tunnel flow conditions with a farfield outer boundary condition was completed first [14]. The plan was to model the wind tunnel test section walls and the full sting structure next to address the goals of this symposium. Unfortunately, time constraints and added computational issues hindered progress leaving the wind tunnel boundary conditions unaddressed. The prediction of the vortex formation and separation was found to be sensitive to several computational parameters and these are described below.

2.0 EXPERIMENTAL AND COMPUTATIONAL METHODOLOGY

2.1 Test Model

The geometry used in the study is the generic Army-Navy Finner (Basic Finner) [15]. The diameter (D_b) of the model is 0.02032 m and has a length (L)-to-diameter ratio (L/D_b) of 10. Figure 2 shows the dimensions normalized with respect to the diameter of the model. The conical forebody has a 10° semi-apex angle and a small nose-tip bluntness ratio of 0.01 to avoid a sharp tip. The whole body was an assembly of three parts, the forebody, the cylinder, and the aft body. The mid-section was mounted on the force balance and the support sting. The fin orientation was kept constant for the current study at Φ_{Fin} = 0° (x) configuration. The fin used in the Basic Finner model is square-planform with a delta cross-section. The fin thickness is $0.08D_b$, the length is $1.0D_b$, and the fin tip bluntness is $0.004D_b$. The trailing end of the support sting was connected to a motorized arc-sector, which was used to vary the incidence angle.

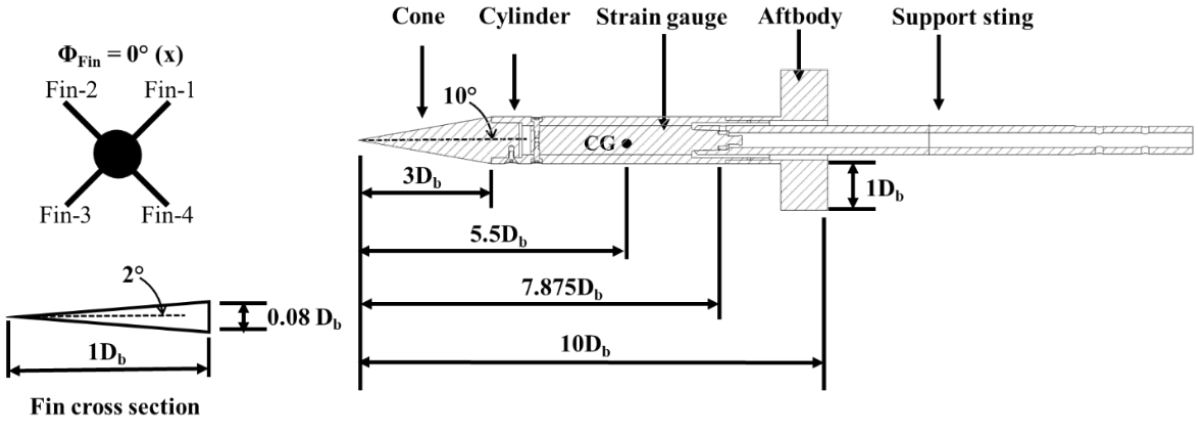

Figure 2: Geometric details of the Basic Finner configuration.

2.2 Wind Tunnel Test Facilities

The experiments were conducted in the Low-Speed Wind-Tunnel (LSWT) facility, located at the Florida Center for Advanced Aero-Propulsion, FAMU-FSU College of Engineering. It is a conventional suction type open-loop wind tunnel driven by a 200 hp motor. The test section dimensions are (height) 0.762 m x (width) 0.762 m x (length) 1.524 m with acrylic windows allowing optical access from all sides. Acrylic material light transmission is > 92 %, and the corresponding refractive index is 1.49. The inlet has a contraction ratio of 9:1 and is fitted with a series of flow conditioners resulting in a low turbulence intensity of less than 0.2%. The freestream velocity can be accurately varied from 2 m/s to 80 m/s and is regulated by changing the motor rpm using a variable frequency drive. The flow angularities in the pitch, $\Delta\alpha$, and in the yaw plane, $\Delta\beta$, of the test section are < 0.05°, measured at the centerline of the tunnel test section. The model was pitched in a way so that it remains in the core of the flow even at high incidence angles to minimize the impact of any flow asymmetries. The velocity is monitored using a pitot-static probe mounted at the test-section entrance (0.68 m upstream of the model location), which does not affect the test-section model blockage. The model was attached to a separately fabricated high alpha adapter fitted to the arc sector assembly shown in Figure 3. A flat surface at the top of the high alpha adapter, which was parallel to the model axis, served as a reference plane for the incidence angle measurement. A digital inclinometer was placed on this flat surface to measure the incidence angle. The arc sector assembly used for pitch control was positioned underneath the test section and passed through a slot in the test section floor. At an incidence angle of 50°, the model nose was more than 0.254 m (12.5D_b) away from the tunnel wall, and hence wall corrections were not necessary. The current study was performed with a tunnel velocity of 40 m/s and at incidence angles from 0° to 60°. The static pressure and temperature were 101.0 kPa and 298 K, respectively.

2.3 Force and Moment Measurements

The force measurements were carried out using a six-component internal force balance (Aerophysics Research Instruments – 0.5 MKXV Internal Balance) for the experimental tests. The force ratings of this balance are 888 N, 444 N, and 222 N for normal, axial, and side-forces, respectively. The moment ratings are 24 N-m, 10 N-m, and 6 N-m for pitching, yaw, and roll-moments, respectively. A National Instruments® (NI) data acquisition card (NI PCIe-8361) was interfaced with a PXIe-1073 chassis, and a NI TB-4330 terminal block to which the force balance was connected. An in-house calibration was performed using calibrated weights to obtain the

calibration coefficients matrix. Data were acquired at 100 Hz for 30 seconds to get a statistically accurate ensemble average.

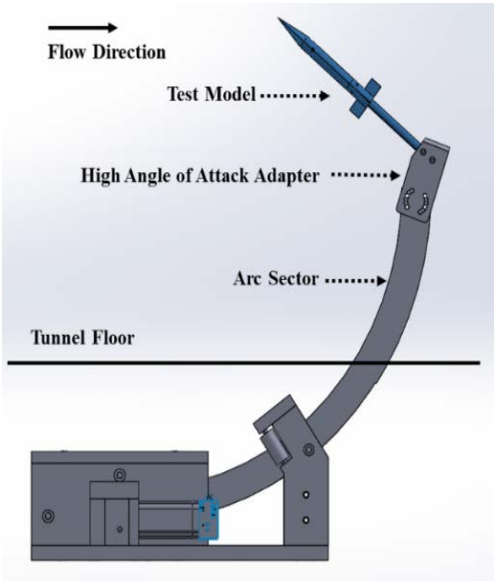

Figure 3: CAD rendering of the Basic Finner model mounted inside the LSWT test-section.

2.4 Particle Image Velocimetry

Planar particle image velocimetry (PIV) was used to obtain quantitative global flow-field information. The flow was seeded using glycol particles having dimensions on the order of 2-5 µm. These particles were illuminated using a Quantum® Nd: YAG 200 mJ double-pulsed laser. The incident ray was focused using a plano-convex spherical lens with a focal length of 1000 mm and fanned into a sheet using a plano-concave cylindrical lens (focal length of 25 mm). The sheet was reflected in the test section using a laser-line mirror (Figure 4). The thickness of the laser sheet in the window of interrogation was approximately 2 mm. Images were acquired using a 5.5-megapixel sCMOS camera having an sCMOS array of 2560 x 2160 pixels. A 180 mm Nikon lens was used to resolve the vortices developing on the body accurately in the present study. The axis of the camera (looking downstream) was set parallel to the model for planes on the slender body. Data were acquired using the DaVis 8.4.0 software, and the time interval between the double pulses was set to 10µs to acquire a mean displacement of ≥ 6 pixels. Statistical ensemble data were acquired at a rate of 15 Hz and a total of 1000 image pairs were acquired. Vector calculations were done using a multi-pass, decreasing correlation window size algorithm. The initial passes had a correlation window size of 64 x 64 pixels with a 50% window overlap. The final passes had a window of 32 x 32 pixels with a 75% overlap. The resulting vector resolution was 0.6 mm, along both axes. For further detailed information on the particle image velocimetry setup, refer to Kumar et al. [16]. Planar PIV was performed at three angles: 38°, 46°, and 48°. For the 38° incidence angle, data was acquired from $z/D_b = 2.84$ (cone-cylinder junction) until aft body end, at every $\Delta z/D_b = 0.25$ intervals, where "z" is the distance along the missile measured from the nose. For 46° and 48° incidence angles, data were acquired at four different locations, $z/D_b = 2.84$, 6.6, 9, and 9.5.

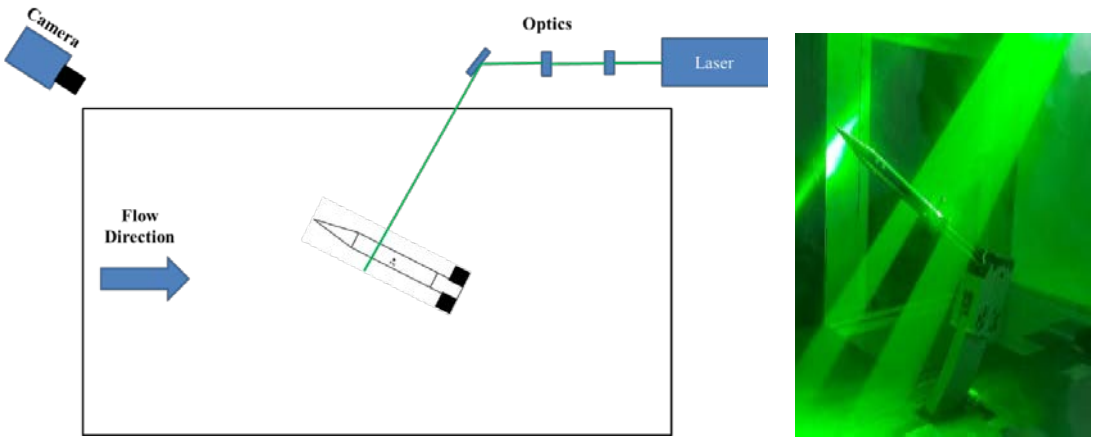

Figure 4: Figures showing a) a schematic of the Particle Image Velocimetry setup and b) laser illuminating the seed particles present in the flow inside the LSWT test-section

2.5 Measurement Uncertainties

The dynamic pressure was recorded using a SETRA Manometer, which has an uncertainty of ± 0.1% of full scale. The uncertainty in the tunnel velocity was determined to be ± 1m/s. The inclinometer used to measure the incidence angle has an error of ±0.05° for the range of 0° to 10°. For incidence angles greater than 10°, the error is ±0.1°. The strain gauge balance has a maximum error of ± 0.2 % of the full scale for all elements. In the present study, uncertainty in side-force was calculated by the method suggested in reference [17]. The measurement uncertainty for the normal force coefficient is ΔCNF = ± 0.02 CNF, side force coefficient is ΔCSF = ± 0.015 CSF, and pitching moment coefficient is ΔCPM = ± 0.02 CPM. The PIV flow-field uncertainty is obtained using the DaVis software, which utilizes the correlation statistics method suggested by Wieneke [18]. Uncertainty is less than 1% except in regions where high-velocity gradients are present.

2.6 Numerical Simulation Methodology

Steady-state Reynolds-Averaged Navier-Stokes (RANS) CFD calculations were performed using the Kestrel Computational Fluid Dynamics (KCFD) unstructured-mesh solver [19] within the Kestrel analysis framework. Kestrel was developed under the U.S. DOD HPCMP initiative to improve DOD acquisition programs using computational science and engineering tools [20]. The result of the initiative is called the Computational Research and Engineering Acquisition Tools and Environments (CREATE) Program, which was established in 2008. The air vehicle portion of CREATE is referred to as CREATE-AV and the high fidelity, fixed-wing vehicle simulation tool is called Kestrel. KCFD is a finite-volume, cell-centered, unstructured flow solver for two-dimensional (2D) and three-dimensional (3D) discretized domains. Meshes can be composed of cells of tetrahedrons, prisms, pyramids, and hexahedrons in 3D or triangles and quadrilaterals in 2D. KCFD employs the Method of Lines using a typical Godunov scheme [21] to compute the spatial residual with second-order accuracy. Various exact and approximate Riemann schemes to compute the fluxes at each element face and up to second-order accuracy is achieved via a sub-iterative point-implicit scheme [22]. The current study used the unstructured, incompressible solver within Kestrel version 10.4.1. The compressible solver within KCFD can be used at this low Mach number; however, it was found that convergence was much faster with the incompressible solver at the higher incidence angles. The implicit local time-stepping scheme with a CFL number of 1000 and 3

Newton sub-iterations was performed at each iteration. Second-order spatial and temporal accurate solver schemes were used, including for the turbulence equation. The Spalart-Allmaras one-equation model with rotation/curvature corrections [23] was used for turbulence modeling closure.

Kestrel also includes a Cartesian-mesh solver, SAMAIR [24], that is used for dual-mesh simulations with solution adaptive mesh refinement (AMR). The Cartesian mesh is connected to the unstructured, near-body (NB) mesh via overset-mesh methodology. The NB mesh can be generated by trimming an existing unstructured mesh to a specified distance from the wall boundaries. The solution proceeds with SAMAIR on the Cartesian mesh and KCFD on the unstructured NB mesh. The original plan was to use the dual mesh approach to take advantage of the efficiency of the AMR. However, the incompressible solver was not available in SAMAIR when the study began and the study proceeded with the unstructured mesh with a refined-mesh region to resolve the vortex structures. Three simulations using the dual-mesh and AMR in Kestrel version 11.1.2 were later completed at the PIV incidence angles.

Unstructured meshes were generated using the Capstone mesh generator [25] developed under the CREATE program. Several meshes were generated in coarse, medium, and fine resolution categories. These meshes were generated over the full domain, with no control of symmetry of the mesh with respect to the longitudinal (vertical) plane of the missile. Figure 5 shows the CFD model, surface mesh, and cut-planes of the volume mesh. A cylindrical section of the sting was modeled (Figure 5a, b). The wind tunnel walls were not modeled; instead, a far-field boundary condition was imposed 20 body lengths ($200D_b$) from the missile body surface. The volume mesh was designed with a series of high-resolution density boxes that enclosed primarily the missile body and leeward side of the missile (Figure 5d-f). The medium-mesh cell edge size was $0.02D_b$ on the body, fin planform, and density boxes enclosing the missile body and fins. The mesh cell size was increased to $0.04D_b$ in the density box enclosing the sting. The cell edge length on the fin leading edge, trailing edge, and tip were $0.001D_b$, $0.007D_b$, and $0.005D_b$, respectively. The total medium-mesh size was 120.1 million cells primarily tetrahedral cells with prismatic cells in the boundary layer. The density boxes extended $2.5D_b$ from the missile body surface in the leeward direction and about $0.9D_b$ in the sideward direction. In the boundary layer region, 26 layers were used with the first cell spacing away from all solid walls set to $0.0004D_b$ for a non-dimensional wall spacing, y+, less than 1.0. A coarse mesh was generated with the values on the missile body, fin planform, and density boxes twice those of the medium mesh listed above resulting in 20.2 million cells. A fine mesh was also generated with values 75% of those listed above resulting in 269.2 million cells. These unstructured meshes were generated over the full domain leaving the likelihood that some asymmetry exists in the mesh that could lead to the development of asymmetric vortex generation. A second medium mesh was generated that was symmetric about the longitudinal (pitch) plane of the missile. Only one-half the computational domain was generated in the mesh generator and then it was mirrored about the pitch plane. The same mesh parameters as in the original medium mesh were used and the total size was 118.2 million cells.

The symmetric medium mesh was used in the dual-mesh, AMR simulations, being trimmed to a distance of $0.3D_b$ from each solid boundary. The average edge length of the cells on the trimmed surface of the NB mesh was $0.017D_b$, which is close to the unstructured-mesh refined density region. This length determines the default finest level of mesh used in the AMR routine, which involved 12 levels in these simulations. The unstructured NB mesh was 18.2 million cells. The final Cartesian mesh sizes in the node-based SAMAIR were 26.9, 24.1, and 32.7 million nodes for the incidence angles of 38°, 46°, and 48°, respectively. The final total degrees of freedom (DOF) were then 45.1, 42.3, and 50.9, respectively. This represents a 60% savings in total mesh DOF compared to the fully unstructured mesh simulations.

The simulations were performed at the same conditions as the wind tunnel test: 40 m/s freestream velocity, 101.0 kPa static pressure, and 298 K static temperature. Simulations were performed at 9 discrete incidence

angles: 5°, 10°, 20°, 30°, 38°, 46°, 48°, 54°, and 60°. These included the three angles with PIV data (38°, 46°, and 48°).

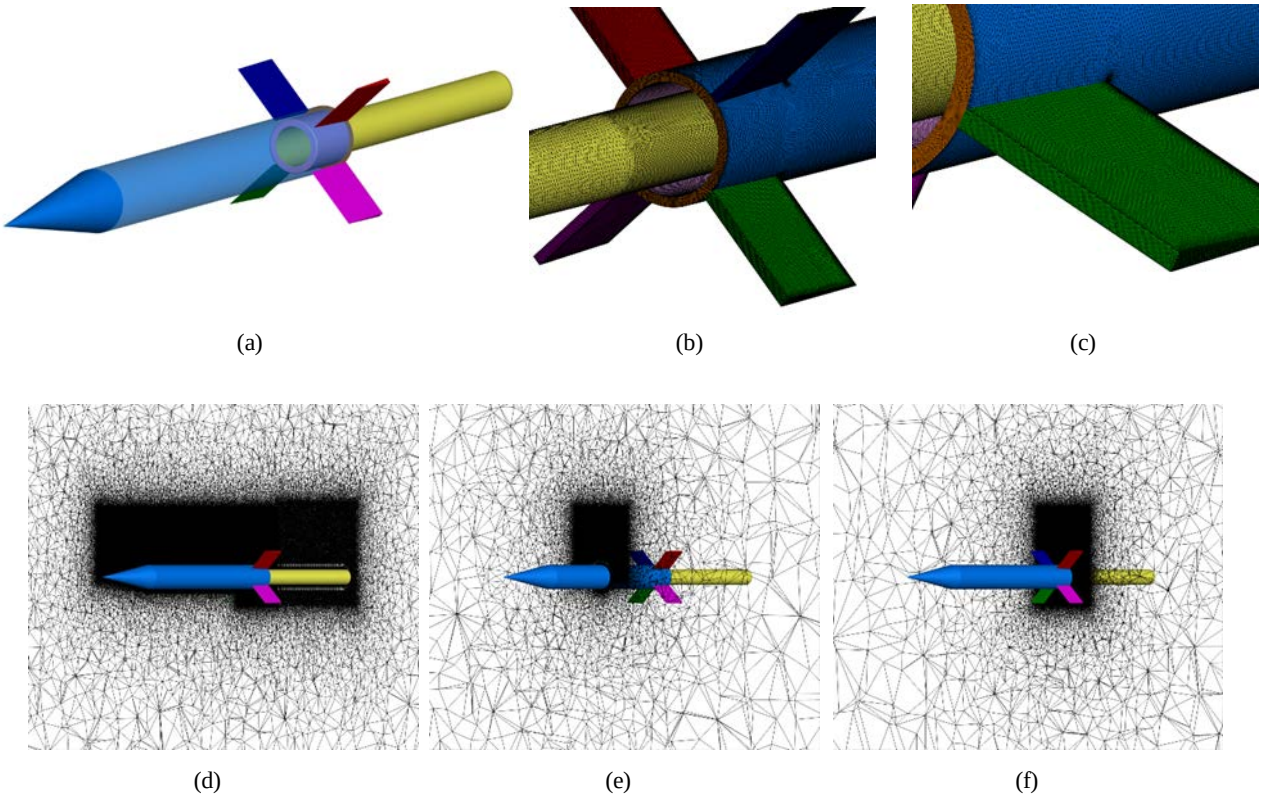

Figure 5: (a) CFD model in Φ_{Fin} = 0° ("x") orientation, (b) close-up view of missile base-sting interface with surface mesh, and (c) close-up view of fin-3 with surface mesh, view of volume mesh on (d) symmetry cut plane, (e) axial plane on the cylindrical region, and (f) axial plane on fin region

3.0 RESULTS AND DISCUSSION

The measured and predicted aerodynamic coefficients of the model are compared in Figures 6–8. Pitching and yawing moments are about the center of gravity of the missile. The plots show the experimental wind tunnel data in two orientations: Φ_{Roll} = 0° and Φ_{Roll} = 180°. These are both "x" orientations of the missile but demonstrate the effect of minor asymmetries in the model fabrication on the generation of the asymmetric vortices (see Figure 7). The predicted results are shown for four meshes: the medium, fine, the symmetric version of the medium mesh, and the dual-mesh AMR using the trimmed, symmetric medium mesh. The coarse mesh, which was not included for clarity, was not adequate to predict the aerodynamics. There is little to no effect of the wind tunnel model orientation nor the mesh characteristics on the longitudinal aerodynamics (Figure 6). The CFD predicts the normal force accurately to α = 20° then underpredicts the wind tunnel value. The flow is either attached or separated consisting of symmetric vortex pairs in the region $\alpha \leq 20°$. The CFD underpredicts the pitching moment (overpredicts stability) even below α = 20°, indicating that the normal force center of pressure is not being predicted accurately. The difference in the predicted and measured pitching moment increases for incidence angles over 20° due to the additional differences in the predicted and measured asymmetric vortex

separation discussed below. The predicted trends are very similar to those observed in the experiment. The normal force increases with incidence angle until about α = 50°, where it then starts to plateau. The pitching moment shows some undulations above α = 30° that correspond to the abrupt changes in lateral loads (Figure 7) in this range. There is little difference between the medium and fine mesh predictions. The predictions using the symmetric medium mesh show some differences above α = 30°, which correspond to differences in the lateral load predictions discussed next. The normal force predictions using the dual mesh with AMR show some differences from the symmetric medium mesh predictions at 38° and 46° incidence, aligning closer to the predictions with the non-symmetric medium mesh. However, these results do not coincide with the trends in the lateral load predictions. Pitching moment predictions show larger differences from both unstructured mesh simulations at these two incidence angles. Excellent prediction of the longitudinal coefficients was previously obtained using the dual-mesh AMR approach for a spinning artillery shell at incidence angles up to 40° [26]. In that case, however, the vortex asymmetry was likely "stabilized" by the spin imparted to the flow via the rotating boundary condition.

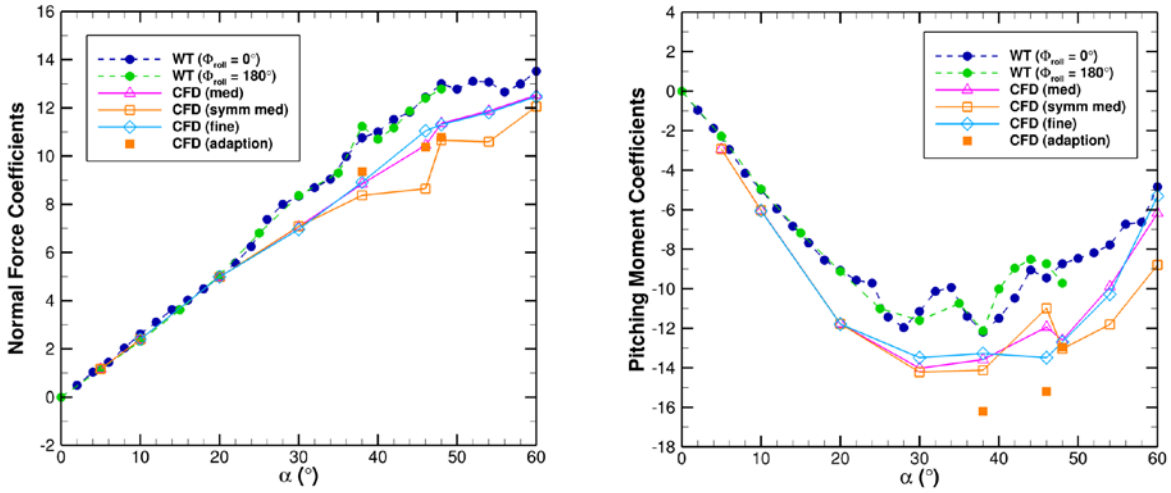

Figure 6: Normal force (left) and pitching moment (right) coefficients with respect to incidence angle.

The lateral load coefficients are most indicative of the nature of the asymmetric vortex shedding and are shown in Figure 7. The side force and yawing moment are very low for α ≤ 20° where the flow either is attached or has symmetric separation. The non-zero lateral loads measured at low angles are due to the measurement uncertainties that are amplified due to the low measured force-to-force balance capacity ratio. The force balance was chosen to accommodate a future supersonic test using the same model and balance for direct comparison with the low-speed experiment. In the experiment, beyond the 20° incidence angle, the side force magnitude increases significantly, accompanied by a periodic variation with several maxima and minima. As will be shown below, in this region the vortices are highly asymmetric, where one vortex is closer to the surface and the other vortex away from the slender body surface. For the experiment in the Φ_{Roll} = 0° roll orientation, the side force magnitude is negative until α = 46° and then at α = 48° it switches to a positive value of significant magnitude. A second side force direction switching is observed between 56° and 60° indicating not only asymmetric vortex shedding but also that a vortex switching process is occurring as incidence angle increases. The periodic variation of side force magnitude and direction will eventually reach a zero net side force beyond the 60° incidence angle. The vortices begin to shed like flow over a bluff body as described in the literature [7]. In

addition to the periodic variation of side force magnitude and direction with the incidence angle, the side force value also changes its sign upon rotating the forebody tip. For the Φ_{Roll} = 180° roll orientation, the side force values are similar at low incidence angles (<20°), but beyond 20°, the side force value changes both in magnitude and direction. As the forebody tip is rotated, the location of imperfections with respect to the incoming flow changes, thereby causing a variation in the side force magnitude and direction. For the Φ_{Roll} = 180° roll orientation, the side force value variation with incidence angle exhibits a similar trend observed in the Φ_{Roll} = 0° roll orientation. The yawing moment shows similar trends as the side force, as expected, but is less sensitive to the changes in the asymmetric vortex shedding.

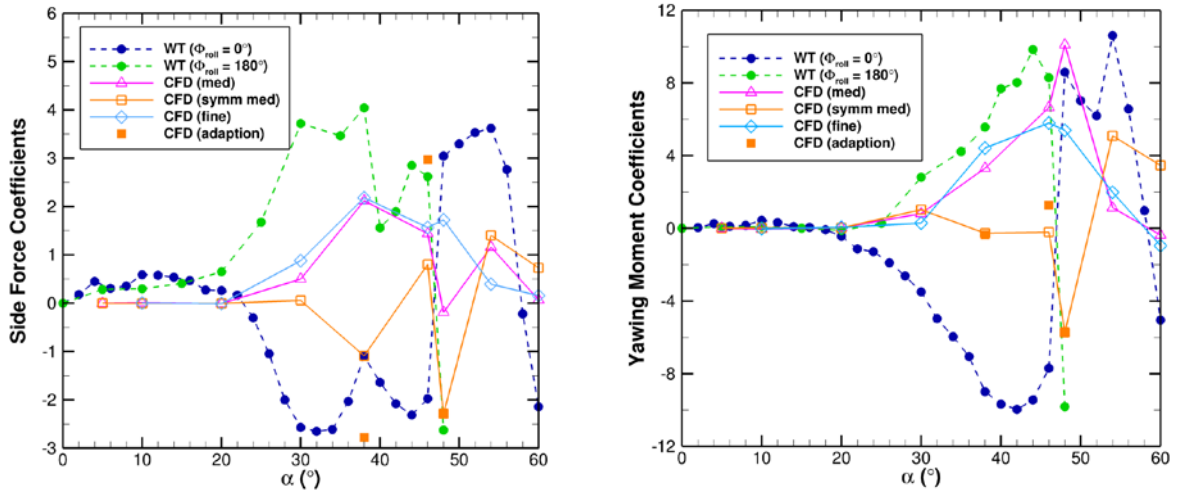

Figure 7: Side force (left) and yawing moment (right) coefficients with respect to incidence angle.

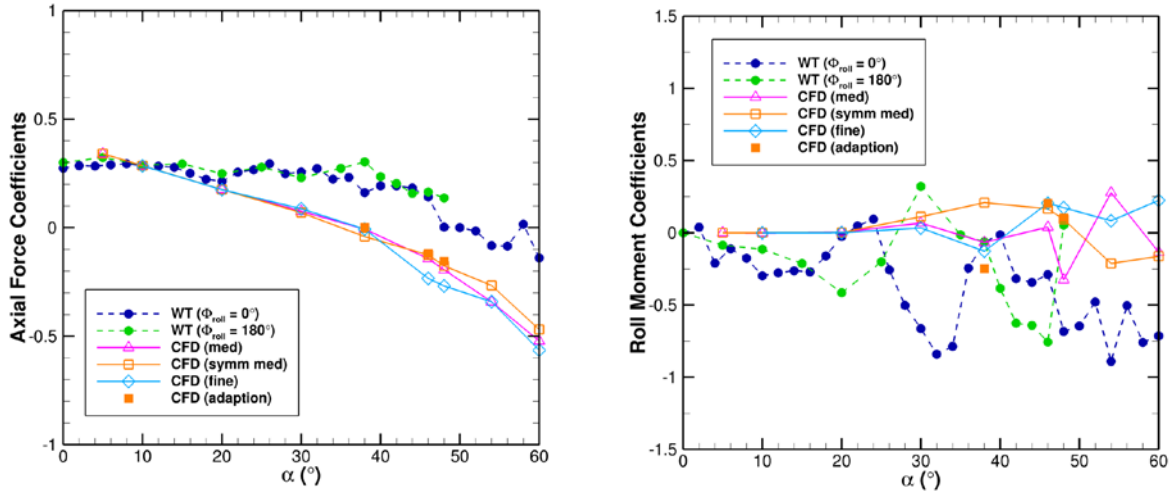

Figure 8: Axial force (left) and rolling moment (right) with respect to incidence angle.

The medium and fine mesh predictions follow the trend of the experimental Φ_{Roll} = 180° side force and yawing moment results—a positive side force and yawing moment prior to switching sign. The inception of asymmetric vortex shedding is delayed in the prediction and the peak side force only reaches about one-half that in the experiment. The medium and fine mesh predict nearly the same side force values up to α = 46°. Above that angle, some mesh dependence appears to exist. The symmetric medium mesh prediction shows asymmetric vortex shedding delayed to above α = 30° and to the opposite side (similar to the Φ_{Roll} = 0° experiment). The predicted yawing moment for the medium and fine meshes appear to match the Φ_{Roll} = 180° experiment reasonably up to about α = 46°. However, this is just by chance, as the differences in side force are likely offset by differences in the predicted side force center of pressure. The dual-mesh AMR predictions of side force show the same trends as those using the symmetric medium mesh (same near-body mesh), with a significantly larger prediction of side force magnitude at the 38° and 46° incidence angles and nearly the same value at 48°. Predictions of yawing moment between the two methods were in closer agreement.

Experimental and predicted axial force and rolling moment are shown in Figure 8. Note that at large angles in separated flow, the axial force can be very low and even negative. The drag force is positive and increases substantially as the normal force component becomes dominant. The predicted values of axial force show a similar trend as the experiment but are underpredicted. These differences are due to (or dominated by) the nature of the predicted vortex shedding compared to the experiment. The predicted rolling moment also compares well to the experiment, although on average overpredicting the rolling moment value. The rolling moment is primarily due to interactions of the shed vortices with tail fins. Very little difference was found in the prediction of axial force and roll moment between the dual-mesh AMR and unstructured methods. The roll moment at 38° incidence angle is of the opposite sign, but the magnitude is very small and sensitive to the difference in the asymmetric shedding.

As incidence angle increases to the high values, the primary vortex pairs will not interact with the fins, but secondary vortices shed from the aft portions of the body can still interact with the fins and generate roll moments, side forces, and yaw moments. This is illustrated in Figure 9, which visualizes the predicted vortex shedding at the three incidence angles with PIV data available. It is observed that even at these high incidence angles, the vortex-fin interaction effect can be significant. Additional analysis can be found in Kumar et al. [14]. The CFD prediction results include the loads on the individual fin components. Future plans include a breakdown of the contribution of the fin components compared to the body to determine the major contributor to the observed asymmetric loads.

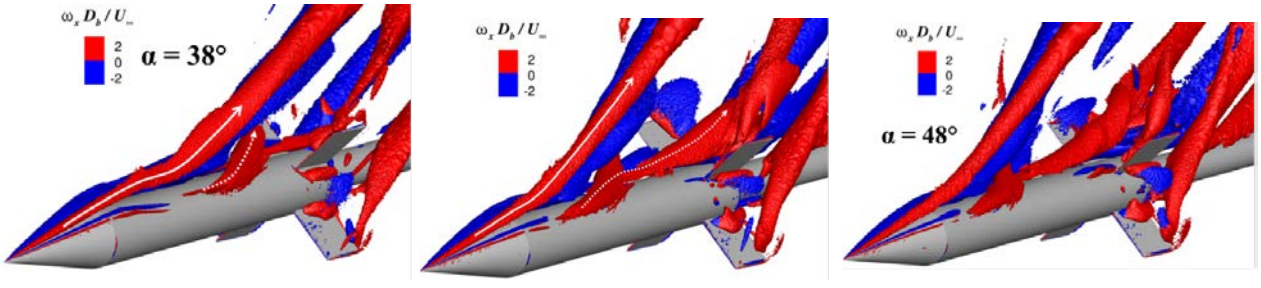

Figure 9: Vorticity Isosurfaces at α = 38°, 46°, and 48° (medium mesh).

The experimental and predicted vorticity flow fields are compared in Figure 10, which shows the nondimensional vorticity field at several selected axial locations on the slender body at α = 38°, as viewed from the nose of the missile. (Coordinate frames differed between the experiment and computation, as indicated by the

axis labels.) Predicted results are shown for both the original medium mesh (Figure 10, middle) and the symmetric medium mesh (Figure 10, right). At this incidence angle, the experimental (Φ_{Roll} = 180°) and predicted side force using the original medium mesh are both at their positive maximum (see Figure 7). Therefore, it is expected that the characteristics of the vortex shedding would be similar. In Figure 10, the vortex structure is illustrated at axial locations of z/D_b = 2.84, 5.3, 6.6, and 8.8. The plots of side force indicate that the predicted vortex asymmetry was delayed relative to that observed in the experiment. In Figure 10, we can see that in the experiment, asymmetric vortex shedding has occurred by z/D_b = 2.84 (the cone-body junction) but the prediction with the medium mesh shows only a small asymmetry in the still attached vortex pair. As we progress down the body to z/D_b = 6.6 and 8.8, the predicted vortex shedding compares qualitatively better with the experiment. These observations suggest the flow separation and vortex asymmetry development occur earlier in the experiments compared to simulations. The progression of vortex shedding for the case of the symmetric medium mesh, on the other hand, shows only a small asymmetry, with little separation from the body until after the z/D_b = 6.6 axial location. The side force coefficient value for this mesh at α = 38° has the opposite sign as the prediction using the original mesh and the experiment. Kumar et al. [14] post-processed the wind tunnel data to show some trajectory plots and peak vorticity values along the trajectory. A similar analysis is in process to analyze the CFD predicted data in the same manner to develop a quantitative comparison of the vortex trajectory characteristics.

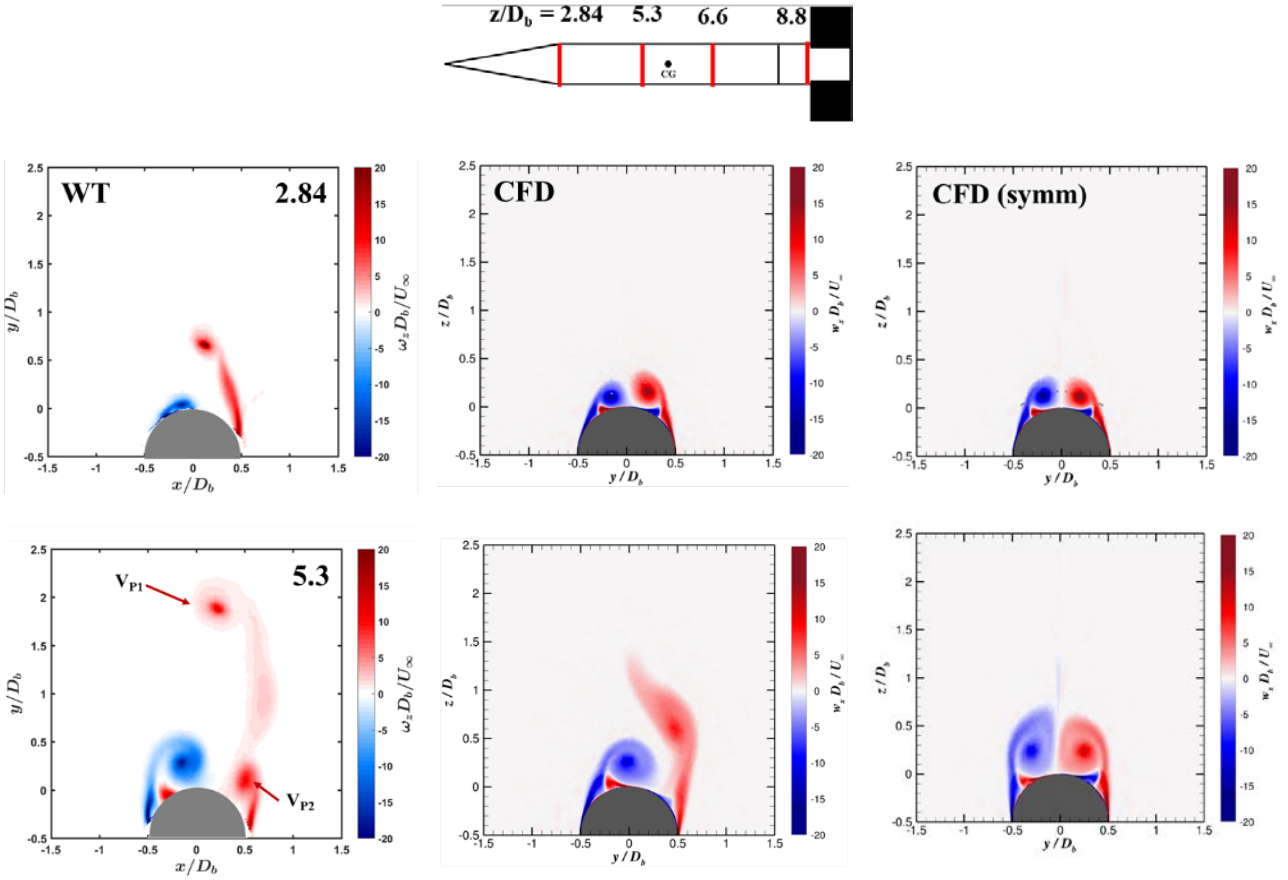

Figure 10: Nondimensional mean vorticity fields at selected locations on the model at α = 38° from wind tunnel (left) and CFD prediction with medium (middle) and symmetric medium (right) meshes.

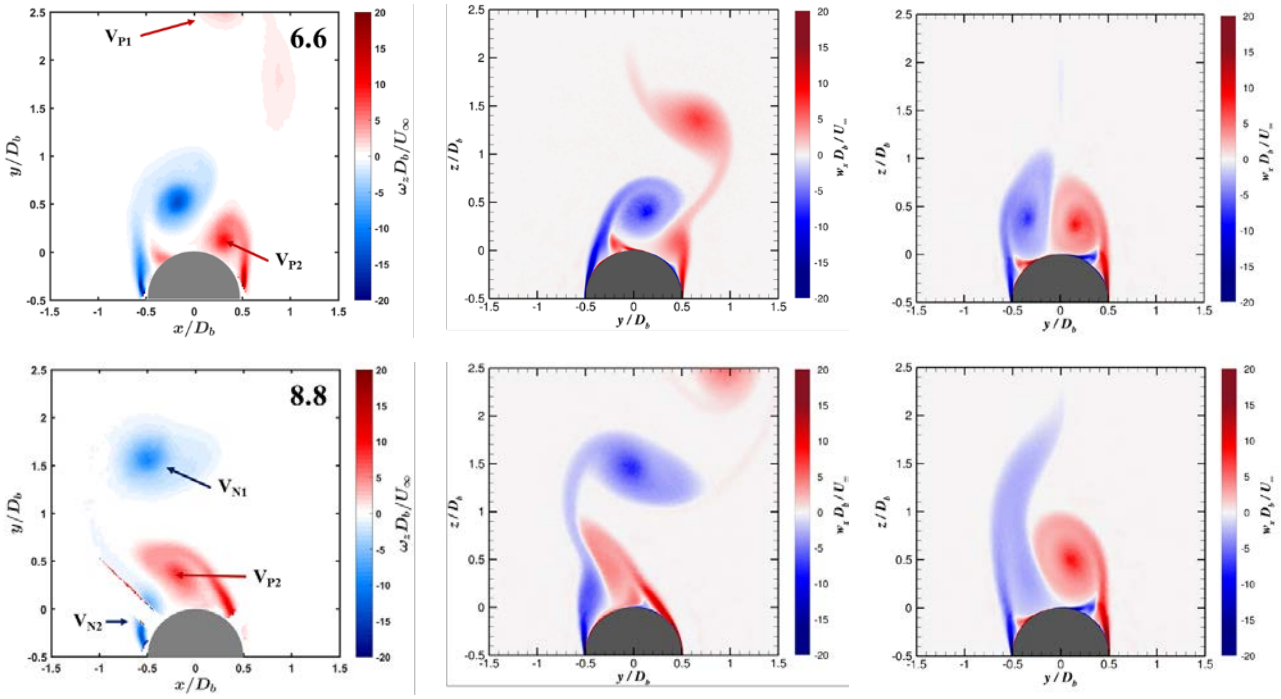

Figure 10 (continued): Nondimensional mean vorticity fields at selected locations on the model at α = 38° from wind tunnel (left) and CFD prediction with medium (middle) and symmetric medium (right) meshes.

The vortical structures predicted in the dual-mesh AMR simulations are now compared to those from the unstructured solution with the symmetric medium mesh. The near-body mesh ($0.3D_b$ from surfaces) is the same and the KCFD solver is used in both cases. The Cartesian solver is used outside this region in the AMR simulations. The minimum cell edge-length in the AMR solution was kept nearly equal to that in the unstructured refined density region of the unstructured mesh ($0.02D_b$), however, the volume of the hexagonal cells is larger than that of the tetrahedral cells. Some differences in the solver methodology between SAMAIR and KCFD also prevent this from being a direct comparison between standard unstructured versus AMR solutions. Figure 11 visualizes the predicted vortex shedding from simulations using the unstructured symmetric medium mesh (top) and the dual-mesh AMR (bottom). The AMR solutions show earlier separation from the body at 38° and 46° incidence angles but similar flow structure evolution at 48°. These flow structures illustrate the reason for the increased side force magnitude at the two lower incidence angles and equivalent magnitude at 48° shown in Figure 7. In a similar manner, the differences in the flow structures predicted using the original (symmetry not enforced) unstructured medium mesh (Figure 9) illustrate the side force magnitude differences observed in Figure 7 compared to the symmetric medium mesh (Figure 11, top). The switching of the sign of the asymmetry between 38° and 46° is also observed in Figure 11.

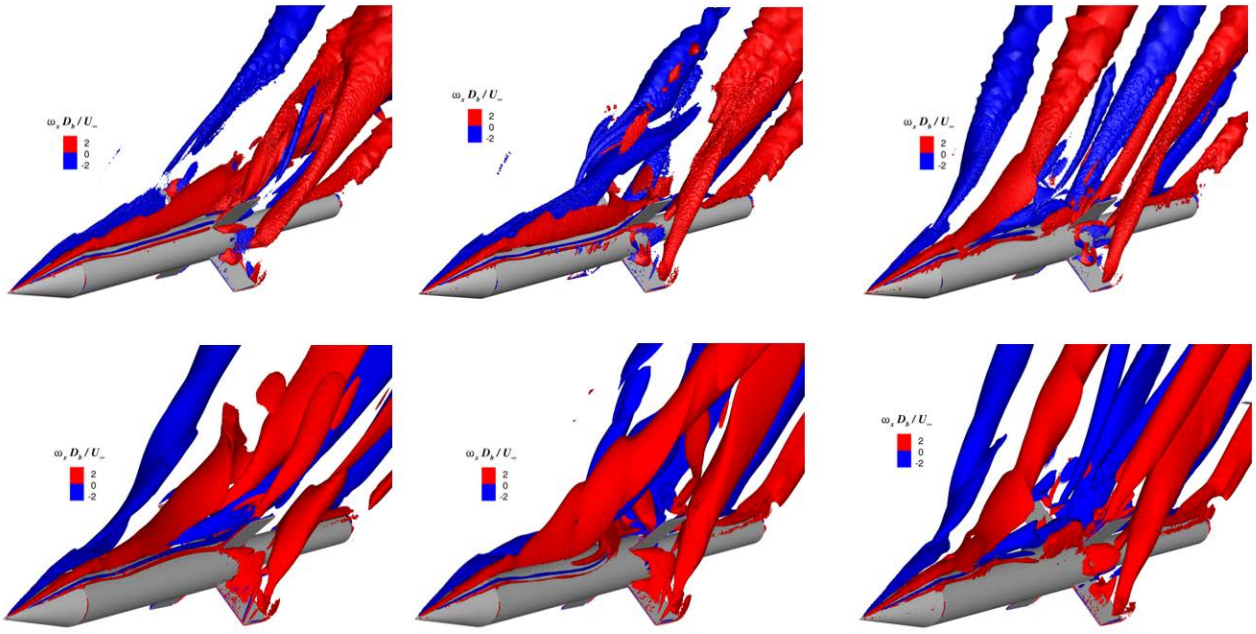

Figure 11: Vorticity Isosurfaces at α = 38°, 46°, and 48° using unstructured symmetric medium mesh (top) and the dual unstructured near-body/Cartesian mesh with AMR.

The nondimensional mean vorticity fields at x/D_b = 6.6 from the unstructured and dual-mesh AMR solutions are compared in Figure 12. Only small differences in asymmetry were observed at x/D_b = 2.84, which is the cone/cylinder junction. The increased asymmetry of the AMR solution (middle row) at 38° and 46° incidence angles is clearly observed. The bottom row of Figure 12 includes the cross-section of the mesh in the AMR solution, including the overset region at $0.3D_b$. The near-body, unstructured mesh was entirely prism layer cells within this region along the cylindrical section of the body. The mesh for the unstructured mesh solution (top row) is too dense to clearly illustrate, but the refined density region with cell edge length $0.02D_b$ filled the region shown. The solutions at 48° incidence angle show a similar structure (and resulting side force, Figure 7) with the AMR solution maintaining the vortex intensity more than that in the unstructured, tetrahedral mesh solution. The adaption region in the AMR solution extended to at least $5D_b$ from the body, nearly twice the window shown.

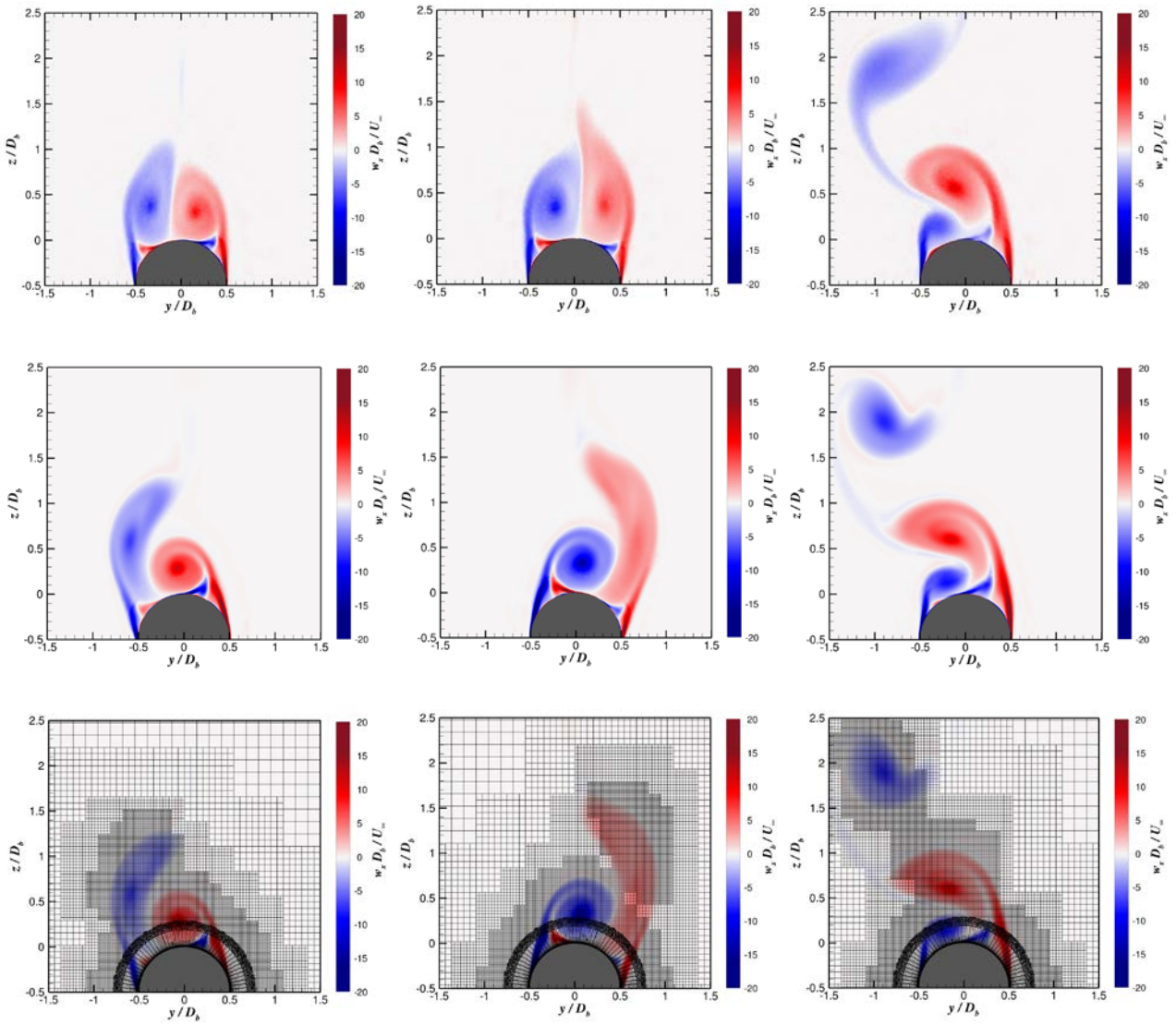

Figure 12: Nondimensional mean vorticity fields at axial location x/D_b = 6.6 using symmetric medium mesh (top) and dual-mesh with AMR method (middle, bottom) at α = 38° (left), 46° (middle), and 48° (right).

4.0 SUMMARY AND CONCLUSIONS

The main objective of the present study is to gain a fundamental understanding of the vortex asymmetry development along the slender body with increasing incidence angles by combining experimental and computational methods. Force measurements showed the normal force coefficient increased consistently with the incidence angle. At low incidence angles (α < 10°), the normal force coefficient variation is linear and varies nonlinearly at high incidence angles. The measured side force coefficient is small at low incidence angles. At high incidence angles, the side force coefficient varies periodically, with a change in magnitude and direction after α = 46°. The derived moments indicate smooth pitch moment characteristics until α = 20°. For α > 20°, the

pitch moment begins to oscillate with increasing incidence angles, as it is significantly affected by the development of vortex asymmetry. Experimental PIV results show the highly asymmetric vortices develop along the slender body and interact with the fins downstream of the aft body. The characteristics of the vortices vary significantly with the incidence angle. It is evident from the present study that the size, strength, and location of the vortices will change with increasing incidence angles. The primary vortices eventually lift off from the slender body surface and are replaced by secondary shear-layer vortices developing from the slender body sides. The primary vortex lift-off location moves upstream along the body with increasing incidence angles. The dissimilar lift-off location between positive and negative primary vortices in conjunction with secondary shear-layer vortices formation leads to a change in the side force magnitude and direction at $\alpha = 48°$ in the experiment. The experimental and simulation flow field comparison shows a mismatch in the vorticity flow field development. A delayed flow field development resulted in underpredicted net forces and moments experienced by the slender body.

The predicted flow field comparisons show a mismatch in the development of the vorticity flow field. The delayed development results in underpredicted net forces and moments experienced on the body. Predictions of all coefficients are reasonably good for $\alpha \leq 20°$ and mesh resolution independence (for the original mesh) was found for $\alpha \leq 46°$. Some of the observed differences in the predicted values of longitudinal and axial loads can be attributed to the difference in the predicted vortex shedding, which is directly indicated by the lateral loads (side force and yawing moment).

The sensitivity of the original instability causing the asymmetric vortex formation was illustrated in both the experimental data and the predictions. In the experiment, rotating the model 180° resulted in an almost symmetric response in the vortex shedding and resulting side force variation with incidence angle. A slight imperfection in the wind tunnel model surface along the nose is assumed to trigger the asymmetry in vortex formation. In the predictions, the original mesh series was generated without ensuring any lateral symmetry of the mesh cells. Therefore, as the crossflow shear layer forms along the missile side surface as incidence angle increases, differences in numerical error in the cells on either side of the body can lead to very small asymmetries in the flow that then grow. In the predictions with the medium mesh that was ensured to be symmetric by mirroring the mesh, the growth of the asymmetric vortex pair was delayed further and resulted in the opposite direction compared to the original mesh. Considering this effect, it would be very difficult to predict the exact nature of the vortex shedding history of the wind tunnel model in this manner. A more controlled asymmetry trigger would have to be used to ensure the asymmetry is initiated at the same location and time in both the experiment and the CFD. For example, a small protuberance located on the nose section that is modeled in the CFD.

In addition to mesh symmetry, the evolution of the asymmetric vortex separation was also influenced by the resolution of the vortex structures away from the solid boundary. This is not surprising, as there can be upstream influences at these flow conditions. This was observed in comparing the predictions using the unstructured symmetric medium mesh and the dual-mesh AMR simulations. The near-body region ($\leq 0.3D_b$) unstructured mesh and solver (KCFD) were the same in both cases but the AMR simulations clearly showed earlier asymmetric separation at the two lower incidence angles. However, another variable in the near-body solution of the AMR was that a newer version of the solver was used. The symmetric unstructured medium mesh simulations will be repeated with the newer version to provide a better comparison of the two methods.

ACKNOWLEDGEMENTS

The authors would like to thank the U.S. Army Research Office for their financial support under contract W911NF-18-1-0462 managed by Dr. Matthew Munson. We are grateful for their support. This study forms a part of a Cooperative Research and Development Agreement (CRADA #17-031-002) established between Army Research Laboratory and FAMU-FSU College of Engineering. This work was supported in part by a grant of high-performance computing time from the U.S. Department of Defense (DOD) High Performance Computing Modernization program at the U.S. Army Research Laboratory DOD Supercomputing Resource Center (DSRC), Aberdeen Proving Ground, MD, the U.S. Air Force DSRC, Wright-Patterson AFB, OH, and the U.S. Army Engineer Research and Development Center DSRC, Vicksburg, MS.

REFERENCES

[1] Auman, L., and Kreeger, R., (1998), "Aerodynamic characteristics of a canard-controlled missile with a free-spinning tail," 36th AIAA Aerospace Sciences Meeting and Exhibit, Reno, NV, January 2020, AIAA-1998-0410.

[2] McDaniel, M., Evans, C., and Lesieutre, D., (2010), "The Effect of Tail Fin Parameters on the Induced Roll of a Canard-Controlled Missile," 28th AIAA Applied Aerodynamics Conference, Chicago, IL, June 2010, AIAA-2010-4226.

[3] Dawson, D., Kumar, R., Kirby, S., Birch, T. J., and Taylor, R., (2018), "Experimental and Numerical Analysis of Fin Effectiveness on an Axisymmetric Configuration," 2018 AIAA Aerospace Sciences Meeting, Kissimmee, FL, January 2018, AIAA-2018-1524.

[4] Porter, S. J. F. C., Chris, and Farnsworth, J., (2012), "Vortex Dynamics of a Tangent Ogive at a High Angle of Attack," 6th AIAA Flow Control Conference, New Orleans, LA, June 2012, AIAA-2012-2953.

[5] Keener, E. R., and Chapman, G. T., (1974), "Onset of Aerodynamic Side Forces at Zero Sideslip on Symmetric Forebodies at High Angles of Attack," AIAA Mechanics and Control of Flight Conference, Anaheim, CA, August 1974, AIAA-1974-0770.

[6] Hunt, B., (1982), "Asymmetric Vortex Forces and Wakes on Slender Bodies," 9th Atmospheric Flight Mechanics Conference, San Diego, CA, August 1982, AIAA-1982-1336.

[7] Ericsson, L. E., and Reding, J. P., (1992), "Asymmetric Flow Separation and Vortex Shedding on Bodies of Revolution," in Hemsch, M. J. (Ed.), Tactical Missile Aerodynamics: General Topics, Progress in Astronautics and Aeronautics, Vol. 141, Washington, D.C., pp. 391–452.

[8] Champigny, P., (1994), "Side forces at high angles of attack: Why, when, how," Recherche Aerospatiale, 269, No. 4.

[9] Taligoski, J., Fernandez, E., Uzun, A., and Kumar, R., (2015), "Study of the Roll Orientation Effects on Vortex Asymmetry on a Conical Forebody at High angles of Incidence," 53rd AIAA Aerospace Sciences Meeting, Kissimmee, FL, January 2015, AIAA-2015-0547.

[10] Kumar, R., Viswanath, P., and Ramesh, O., (2005), "Nose Bluntness for Side Force Control on Circular Cones at High Incidence," Journal of Aircraft, Vol. 42, No. 5, pp. 1133–1141.

[11] Erickson, G., and Brandon, J., (1987), "On the nonlinear aerodynamic and stability characteristics of a generic chine-forebody slender-wing fighter configuration," 5th Applied Aerodynamics Conference, Monterey, CA, August 1987, AIAA-1987-2617.

[12] Blair, A. B, (1978), "Wind Tunnel Investigation at Supersonic Speeds of a Controlled Canard Missile with Fixed and Free-Rolling Tail Fins," NASA Technical Paper 1316, September 1978.

[13] Kumar, R., Ghua, T. K., Kumar, R., and DeSpirito, J., (2020), "Experimental and Numerical Study of Forebody Vortex Interactions on a Generic Axisymmetric Finned Configuration," AIAA SciTech 2020 Forum,

Orlando, FL, January 2020, AIAA-2020-1991.

[14] Kumar, R., Kumar, R., and DeSpirito, J., (2021) "Experimental and Numerical Investigation of the Vortex Asymmetry on the Basic Finner Configuration," AIAA SciTech 2021 Forum, virtual conference, January 2021, AIAA-2021-0025.

[15] Dupuis, A., (2002), "Aeroballistic Range and Wind Tunnel Tests of the Basic Finner Reference Projectile from Subsonic to High Supersonic Velocities," Defense R&D Canada Valcartier, TM 2002-136, October 2002.

[16] Kumar, R., Guha, T.K. & Kumar, R., (2020), "Role of secondary shear-layer vortices in the development of flow asymmetry on a cone–cylinder body at high angles of incidence," Experiments in Fluids 61, 215.

[17] Mahadevan, S., Rodriguez, J., and Kumar, R., (2018), "Effect of Controlled Imperfections on the Vortex Asymmetry of a Conical Body," AIAA Journal, Vol. 56, No. 9, pp. 3460–3477.

[18] Wieneke, B., (2015) "PIV uncertainty quantification from correlation statistics", Measurement Science and Technology, Volume 26.

[19] McDaniel, D. R., Nichols, R., Eymann, T., Starr, R., Morton, S., (2016), "Accuracy and Performance Improvements to Kestrel's Near-Body Flow Solver," 54th AIAA Aerospace Sciences Meeting, San Diego, CA, January 2016, AIAA-2016-1051.

[20] McDaniel, D. R., and Morton, S. A., (2018), "HPCMP CREATE-AV Kestrel Architecture, Capabilities, and Future Directions," 2018 AIAA Aerospace Sciences Meeting, Kissimmee, FL, January 2018, AIAA-2018-0025.

[21] Godunov, S., (1959), "A Finite Difference Method for the Numerical Calculation of Discontinuous Solutions of the Equations of Fluid Dynamics," Matematicheskii Sbornik, Vol. 47, spp. 271–290.

[22] Tomaro, R. F., Strang, W. Z., and Sankar, L. N., (1997), "An Implicit Algorithm for Solving Time Dependent Flows on Unstructured Grids," 35th AIAA Aerospace Sciences Meeting, Reno, NV, January 1997, AIAA-1997-0333.

[23] Spalart, P. R., and Shur, M., (1997), "On the Sensitization of Turbulence Models to Rotation and Curvature," Aerospace Science and Technology, Vol. 5, pp. 297–302.

[24] Eymann, T. A., Nichols, R. H., McDaniel, D. R., and Tuckey, T. R., "Cartesian Adaptive Mesh Refinement with HPCMP CREATE-AV Kestrel Solver," AIAA SciTech 2015 Forum, Kissimmee, FL, January 2015, AIAA-2015-0040.

[25] Mestreau, E., Aubry, R., Dey, S., and Richardson, M., (2019), "CREATE-MG Capstone: Design, Architecture & Feature Modelling Improvements," AIAA SciTech 2019 Forum, San Diego, CA, January 2019, AIAA-2019-1716.

[26] DeSpirito, J., "CFD Aerodynamic Characterization of 155-mm Projectile at High Angles-of-Attack," AIAA AVIATION Forum, Denver, CO, June 2017, AIAA-2017-3397.